Shock Wave Analysis of Supersonic Flow over a Two-Dimensional Wedge

Kaitaro Hori*
University of California, Davis, Davis, CA, 95616

This report investigates oblique shock formation over a two-dimensional wedge in supersonic flow. Shock wave angles are compared using Schlieren images, analytical oblique-shock theory, and ANSYS Fluent Mach number contours for freestream Mach numbers of 2.0, 2.5, and 3.0 with wedge half-angles of 5°, 10°, and 15°. The theoretical shock angles and downstream flow properties are calculated using the θ–β–M relation and normal-shock relations applied to the normal component of the upstream Mach number. Experimental shock angles are measured from the provided Schlieren images, while computational shock angles are measured from the CFD Mach contours. The results are presented using comparison tables, side-by-side Schlieren/CFD figures, and a θ–β–M plot.

Nomenclature

M_1	=	Freestream Mach number
M_2	=	Downstream Mach number behind the oblique shock
M_{n1}	=	Upstream Mach number normal to the shock
M_{n2}	=	Downstream Mach number normal to the shock
p_1	=	Freestream static pressure, Pa
p_2	=	Downstream static pressure behind the shock, Pa
$p_{0,2}$	=	Downstream total pressure behind the shock, Pa
T_1	=	Freestream static temperature, K
T_2	=	Downstream static temperature behind the shock, K
ρ_1	=	Freestream density, kg/m^3
ρ_2	=	Downstream density behind the shock, kg/m^3
θ	=	Wedge half-angle or flow deflection angle, deg
β	=	Oblique shock angle measured from the freestream direction, deg
Δ_{shock}	=	Included angle between upper and lower shock lines, deg
γ	=	Ratio of specific heats
Subscripts		
CFD	=	Computational fluid dynamics result
exp	=	Experimental result measured from Schlieren image
theory	=	Analytical weak-shock result

I. Introduction

Supersonic flow over a wedge produces an attached oblique shock when the flow is turned through the wedge angle. Across the shock, pressure, temperature, and density increase, while Mach number decreases. Because the density gradient across the shock is large, the shock can be visualized using Schlieren photography. The objective of this project is to compare shock angles measured from experimental images and CFD results with the theoretical θ–β–M relation. The conditions considered in the study are summarized in Table 1.

*Undergraduate Student, Department of Mechanical and Aerospace Engineering.

Table 1 Flow conditions considered in this study.

Case	M_1	θ	Freestream Conditions
1	2.0	5°	$p_1 = 101\,325$ Pa, $T_1 = 300$ K
2	2.0	10°	$p_1 = 101\,325$ Pa, $T_1 = 300$ K
3	2.0	15°	$p_1 = 101\,325$ Pa, $T_1 = 300$ K
4	2.5	5°	$p_1 = 101\,325$ Pa, $T_1 = 300$ K
5	2.5	10°	$p_1 = 101\,325$ Pa, $T_1 = 300$ K
6	2.5	15°	$p_1 = 101\,325$ Pa, $T_1 = 300$ K
7	3.0	5°	$p_1 = 101\,325$ Pa, $T_1 = 300$ K
8	3.0	10°	$p_1 = 101\,325$ Pa, $T_1 = 300$ K
9	3.0	15°	$p_1 = 101\,325$ Pa, $T_1 = 300$ K

II. Theory

A. Oblique-Shock Relation

For a steady, two-dimensional wedge flow, the wedge half-angle θ, shock angle β, and freestream Mach number M_1 are related by

$$\tan\theta = 2\cot\beta\left[\frac{M_1^2\sin^2\beta - 1}{M_1^2(\gamma + \cos 2\beta) + 2}\right]. \tag{1}$$

Air is modeled as a calorically perfect gas with $\gamma = 1.4$. For a given M_1 and θ, Eq. (1) can produce weak and strong oblique-shock solutions. The weak-shock branch is used in this report because it is the attached solution normally observed for wedge flows.

B. Post-Shock Relations

The upstream Mach number normal to the shock is

$$M_{n1} = M_1 \sin\beta. \tag{2}$$

The static pressure ratio, density ratio, and static temperature ratio are calculated as

$$\frac{p_2}{p_1} = 1 + \frac{2\gamma}{\gamma + 1}\left(M_{n1}^2 - 1\right), \tag{3}$$

$$\frac{\rho_2}{\rho_1} = \frac{(\gamma + 1)M_{n1}^2}{(\gamma - 1)M_{n1}^2 + 2}, \tag{4}$$

$$\frac{T_2}{T_1} = \frac{p_2/p_1}{\rho_2/\rho_1}. \tag{5}$$

The downstream normal Mach number and downstream Mach number are

$$M_{n2}^2 = \frac{1 + \frac{\gamma-1}{2}M_{n1}^2}{\gamma M_{n1}^2 - \frac{\gamma-1}{2}}, \tag{6}$$

$$M_2 = \frac{M_{n2}}{\sin(\beta - \theta)}. \tag{7}$$

III. Methodology

A. Experimental Shock-Angle Measurement

The experimental shock angles were measured from the Schlieren images. The wedge tip and freestream centerline were identified in CAD. Lines were drawn along the visible upper and lower shock structures. When both shock lines were clear, the included angle between the shock lines was measured as Δ_{shock}, and the experimental shock angle was calculated as

$$\beta_{\text{exp}} = \frac{\Delta_{\text{shock}}}{2}. \tag{8}$$

If one side of the shock was less clear because of image blur or contrast near the wedge tip, the clearer side was used as the primary reference.

B. Analytical Calculation Procedure

All analytical values were calculated from Eqs. (1)–(7). Equation (1) was solved for the weak-shock value of β_{theory} for each case. The normal component of the upstream Mach number and the post-shock properties were then calculated from the normal-shock relations. One representative hand calculation is included in Appendix A.

C. Computational Result Processing

The computational results were processed from the ANSYS Fluent Mach number contour screenshots. Each screenshot was cropped to remove excess white space and enlarge the flow field. The oblique shock was identified as the narrow transition band separating the upstream red region and downstream blue region. A line was fitted through the center of the shock band, and the angle between that line and the freestream direction was reported as β_{CFD}.

IV. Results and Discussion

A. Analytical Oblique-Shock Results

The analytical weak-shock results are summarized in Table 2. The pressure and temperature values are presented in SI units.

Table 2 Theoretical oblique-shock results.

M_1	θ	β_{theory}	M_{n1}	M_2	p_2 [Pa]	T_2 [K]	$p_{0,2}$ [Pa]
2.0	5°	34.30°	1.127	1.821	133284	324.6	791150
2.0	10°	39.31°	1.267	1.641	172919	351.0	780638
2.0	15°	45.34°	1.423	1.446	222373	380.8	755040
2.5	5°	27.42°	1.151	2.292	139823	329.2	1725357
2.5	10°	31.85°	1.319	2.086	188857	360.9	1689494
2.5	15°	36.94°	1.503	1.874	250019	396.6	1608237
3.0	5°	23.13°	1.179	2.750	147325	334.4	3702145
3.0	10°	27.38°	1.380	2.505	208169	372.5	3584542
3.0	15°	32.24°	1.600	2.255	285895	416.5	3331304

B. Experimental Shock-Angle Results

Table 3 summarizes the Schlieren-image measurements. The experimental measurements are in degrees because the θ–β–M chart and the wedge half-angles are conventionally reported in degrees.

C. Computational Shock-Angle Results

Table 4 lists the shock angles measured from the CFD Mach contours. The fitted shock centerline gives CFD angles close to the analytical weak-shock predictions for all nine cases.

Table 3 Experimental shock-angle measurements from Schlieren images.

M_1	θ	Δ_{shock}	β_{exp}
2.0	5°	76.34°	38.17°
2.0	10°	74.78°	37.39°
2.0	15°	80.42°	40.21°
2.5	5°	63.28°	31.64°
2.5	10°	61.16°	30.58°
2.5	15°	63.16°	31.58°
3.0	5°	53.86°	26.93°
3.0	10°	52.84°	26.42°
3.0	15°	55.26°	27.63°

Table 4 Computational shock-angle measurements from CFD Mach contours.

M_1	θ	β_{theory}	β_{CFD}
2.0	5°	34.30°	34.174°
2.0	10°	39.31°	39.145°
2.0	15°	45.34°	45.253°
2.5	5°	27.42°	27.546°
2.5	10°	31.85°	31.810°
2.5	15°	36.94°	36.913°
3.0	5°	23.13°	22.410°
3.0	10°	27.38°	27.166°
3.0	15°	32.24°	32.155°

D. θ–β–M Comparison

Figure 1 compares the theoretical weak-shock curves with the experimental and CFD shock-angle measurements. The CFD points fall close to the theoretical weak-shock curves, indicating that the numerical simulations captured the attached oblique-shock geometry accurately. The experimental measurements follow the same overall trend, but show larger scatter due to finite shock thickness, image blur, and uncertainty in selecting the exact shock centerline from the Schlieren images.

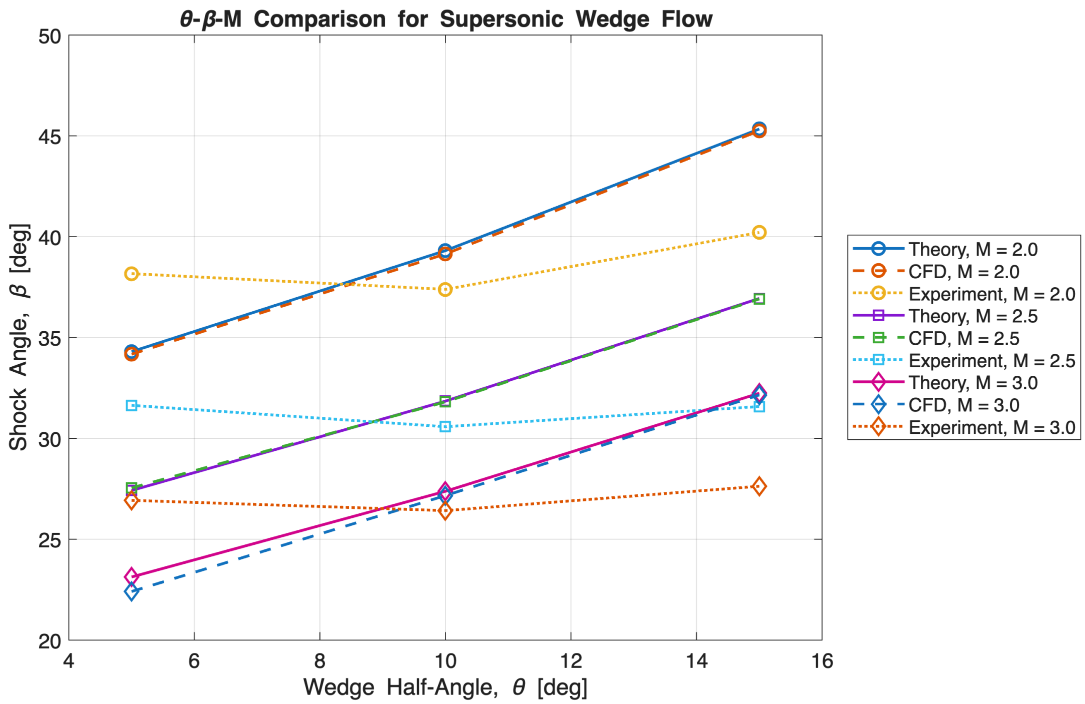

Fig. 1 θ–β–M **comparison between theory, Schlieren-image measurements, and CFD measurements.**

E. Shock-Angle Error Comparison

The percent error is calculated relative to the analytical weak-shock solution:

$$\% \text{ error} = \frac{|\beta_{\text{measured}} - \beta_{\text{theory}}|}{\beta_{\text{theory}}} \times 100. \tag{9}$$

The resulting comparison is given in Table 5.

‘‘‘

F. Schlieren and CFD Figure Comparison

The following figures compare the Schlieren images and CFD Mach contours for each simulated condition.

Table 5 Shock-angle comparison between theory, experiment, and CFD.

M_1	θ	β_{theory}	β_{exp}	Exp. Error [%]	β_{CFD}	CFD Error [%]
2.0	5°	34.30°	38.17°	11.28	34.174°	0.37
2.0	10°	39.31°	37.39°	4.88	39.145°	0.42
2.0	15°	45.34°	40.21°	11.31	45.253°	0.19
2.5	5°	27.42°	31.64°	15.39	27.546°	0.46
2.5	10°	31.85°	30.58°	3.99	31.810°	0.13
2.5	15°	36.94°	31.58°	14.51	36.913°	0.07
3.0	5°	23.13°	26.93°	16.43	22.410°	3.11
3.0	10°	27.38°	26.42°	3.51	27.166°	0.78
3.0	15°	32.24°	27.63°	14.30	32.155°	0.26

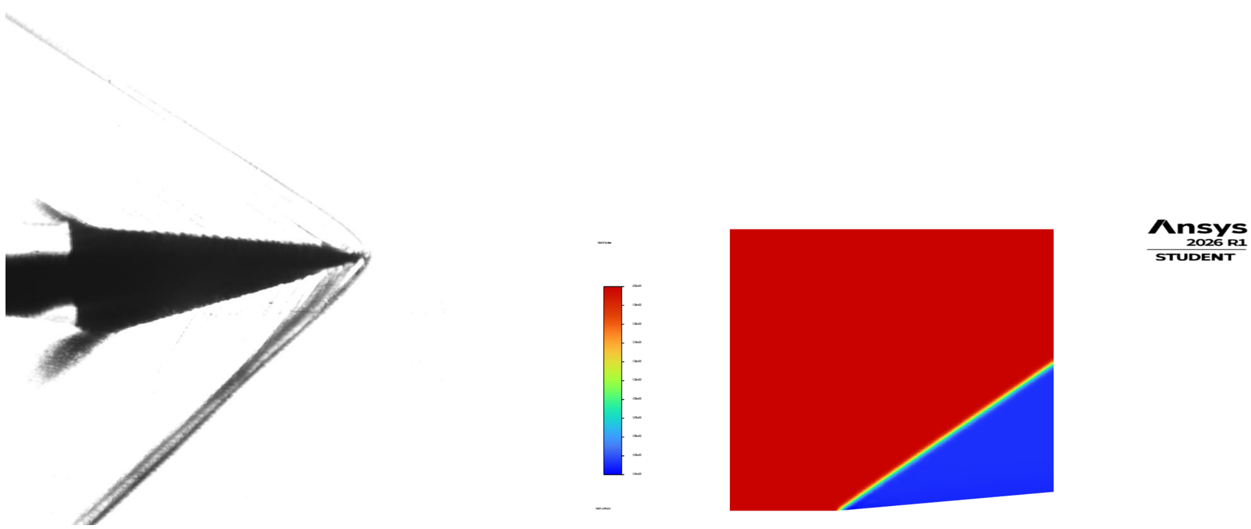

Schlieren image CFD Mach contour

Fig. 2 Schlieren and CFD comparison for $M_1 = 2.0$ and $\theta = 5°$.

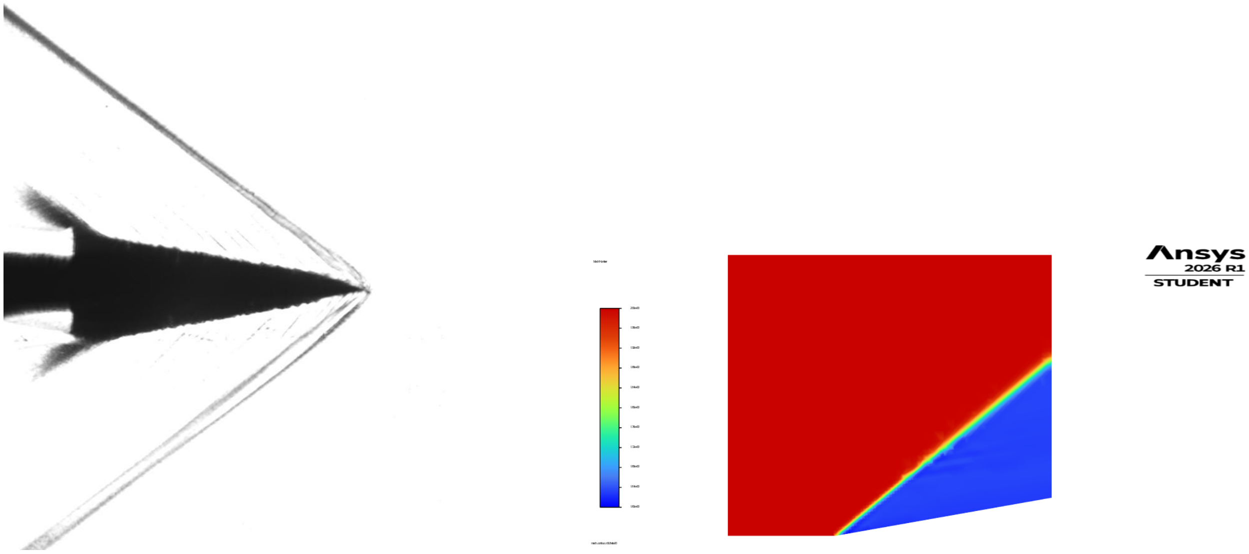

Schlieren image CFD Mach contour

Fig. 3 Schlieren and CFD comparison for M_1 = 2.0 and θ = 10°.

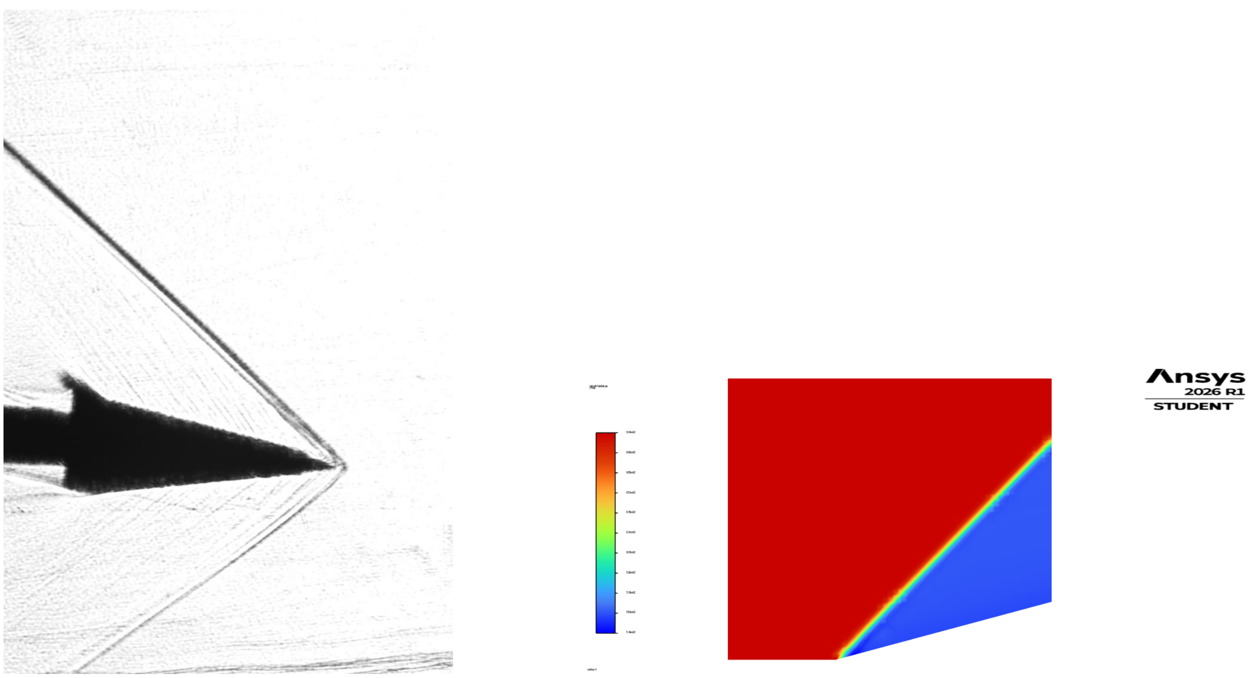

Schlieren image CFD Mach contour

Fig. 4 Schlieren and CFD comparison for M_1 = 2.0 and θ = 15°.

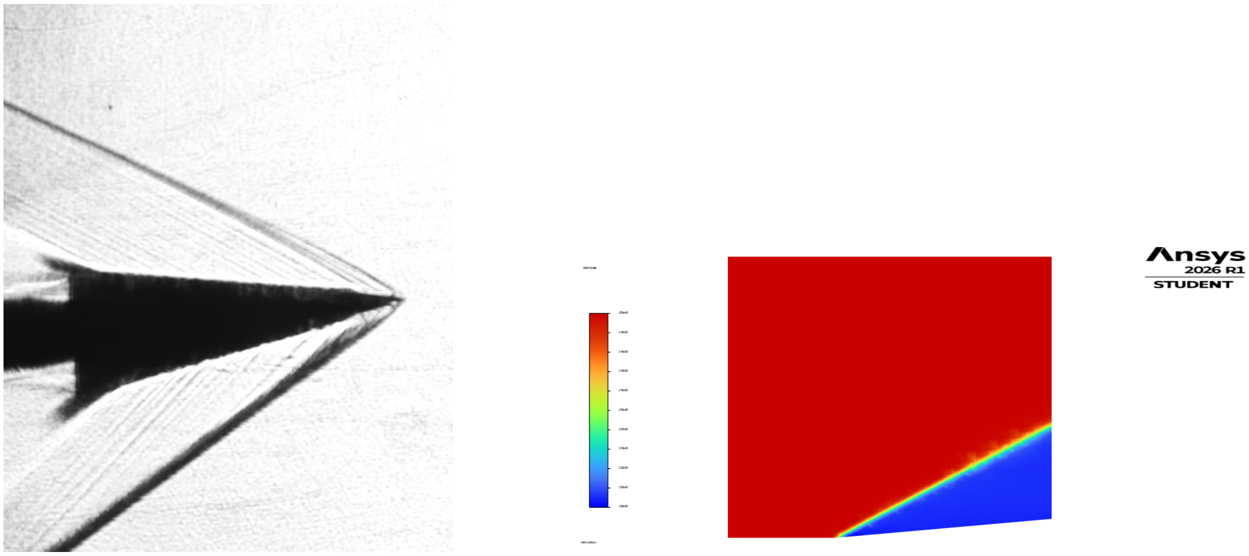

Schlieren image | CFD Mach contour

Fig. 5 Schlieren and CFD comparison for $M_1 = 2.5$ and $\theta = 5°$.

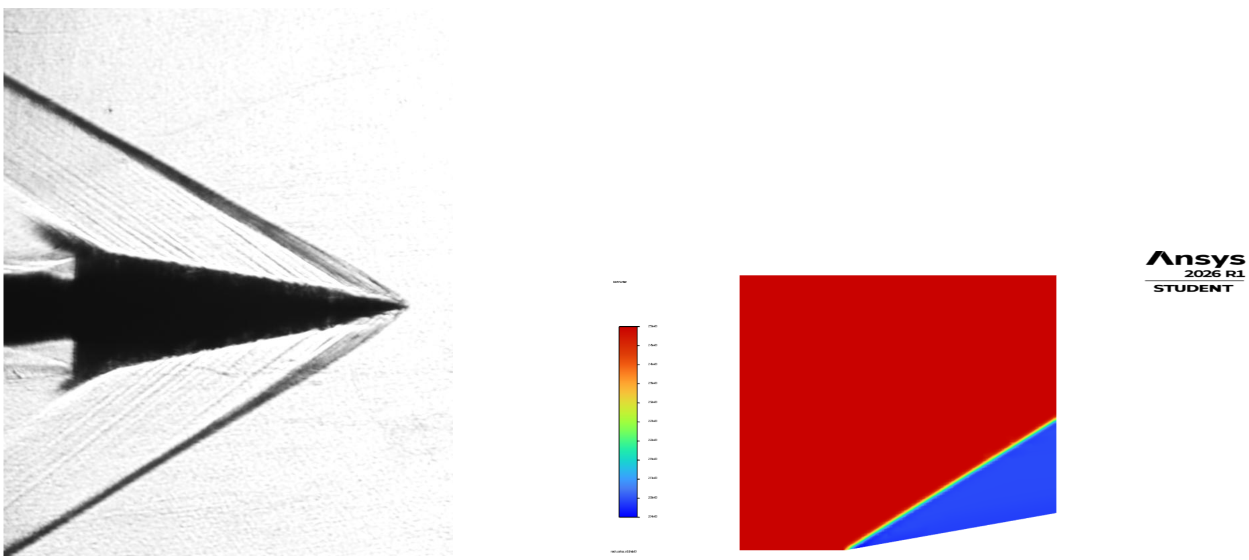

Schlieren image | CFD Mach contour

Fig. 6 Schlieren and CFD comparison for $M_1 = 2.5$ and $\theta = 10°$.

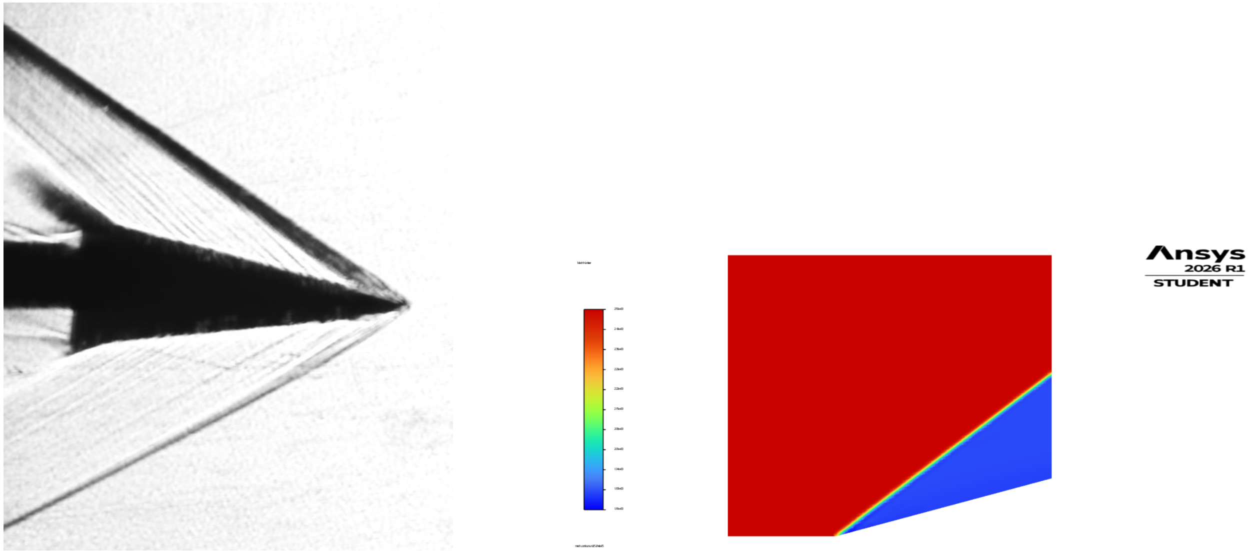

Schlieren image CFD Mach contour

Fig. 7 Schlieren and CFD comparison for $M_1 = 2.5$ and $\theta = 15°$.

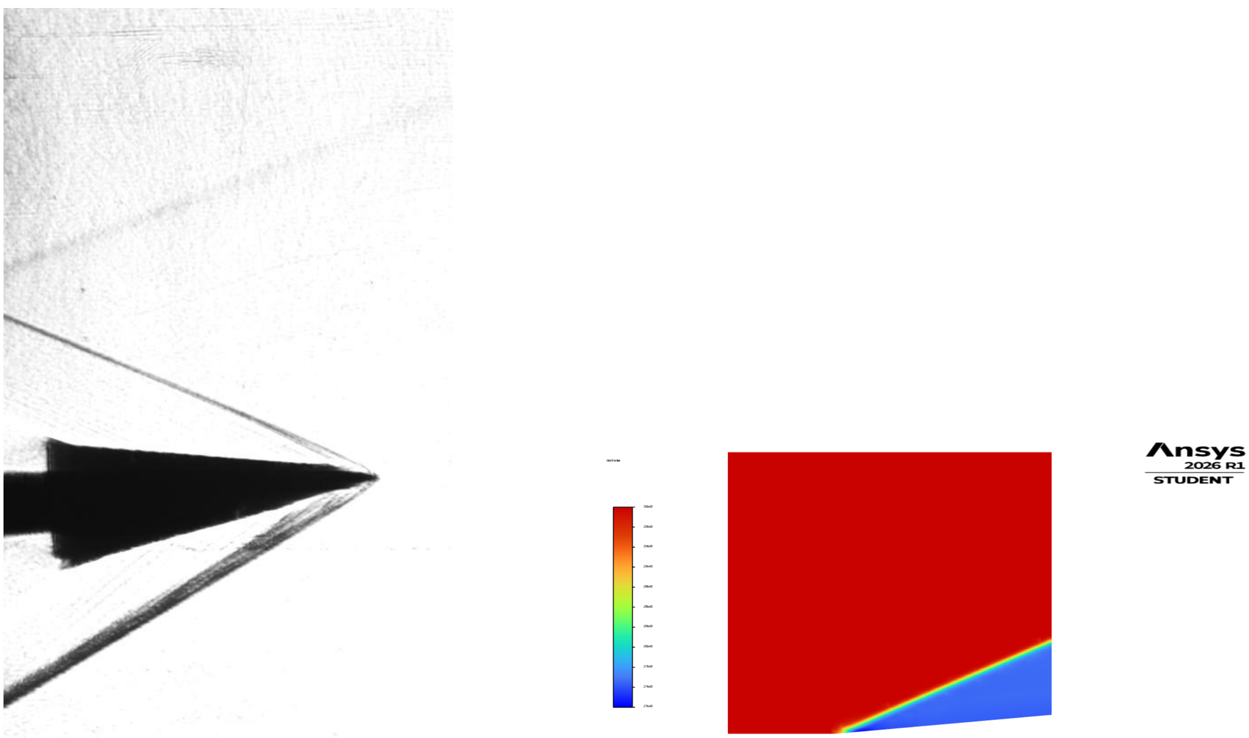

Schlieren image CFD Mach contour

Fig. 8 Schlieren and CFD comparison for $M_1 = 3.0$ and $\theta = 5°$.

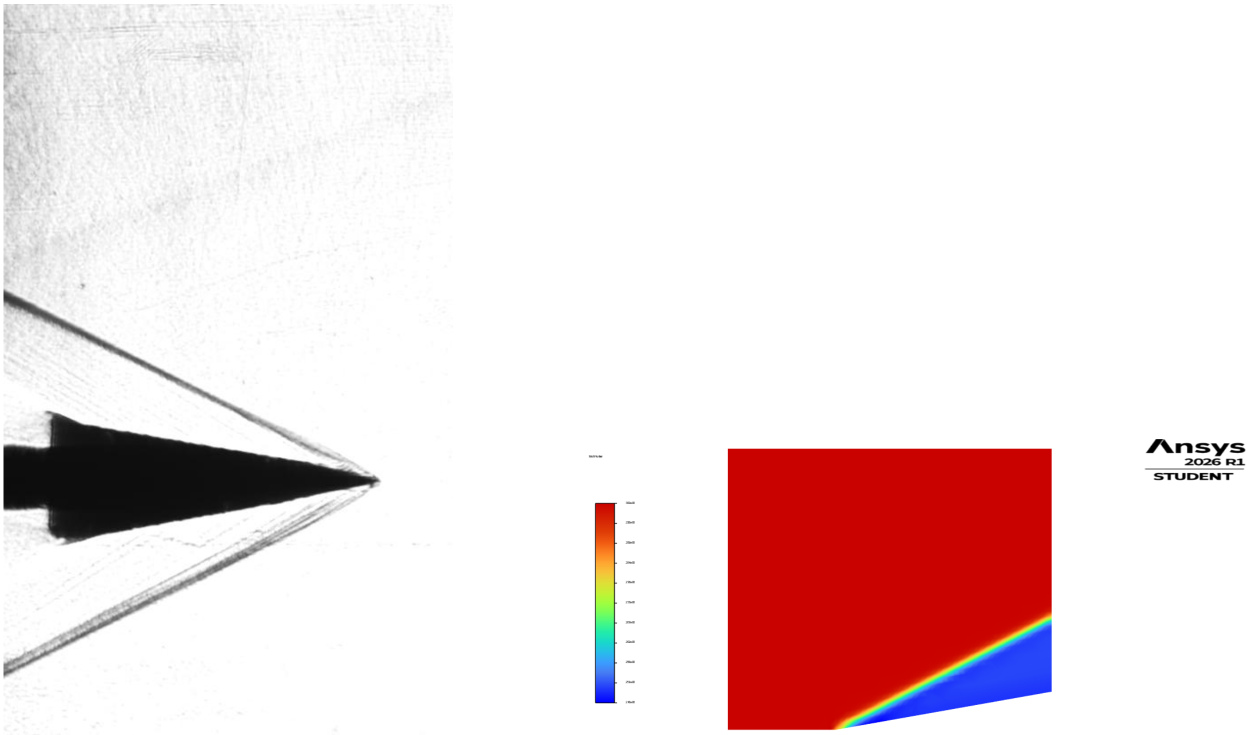

Schlieren image CFD Mach contour

Fig. 9 Schlieren and CFD comparison for $M_1 = 3.0$ and $\theta = 10°$.

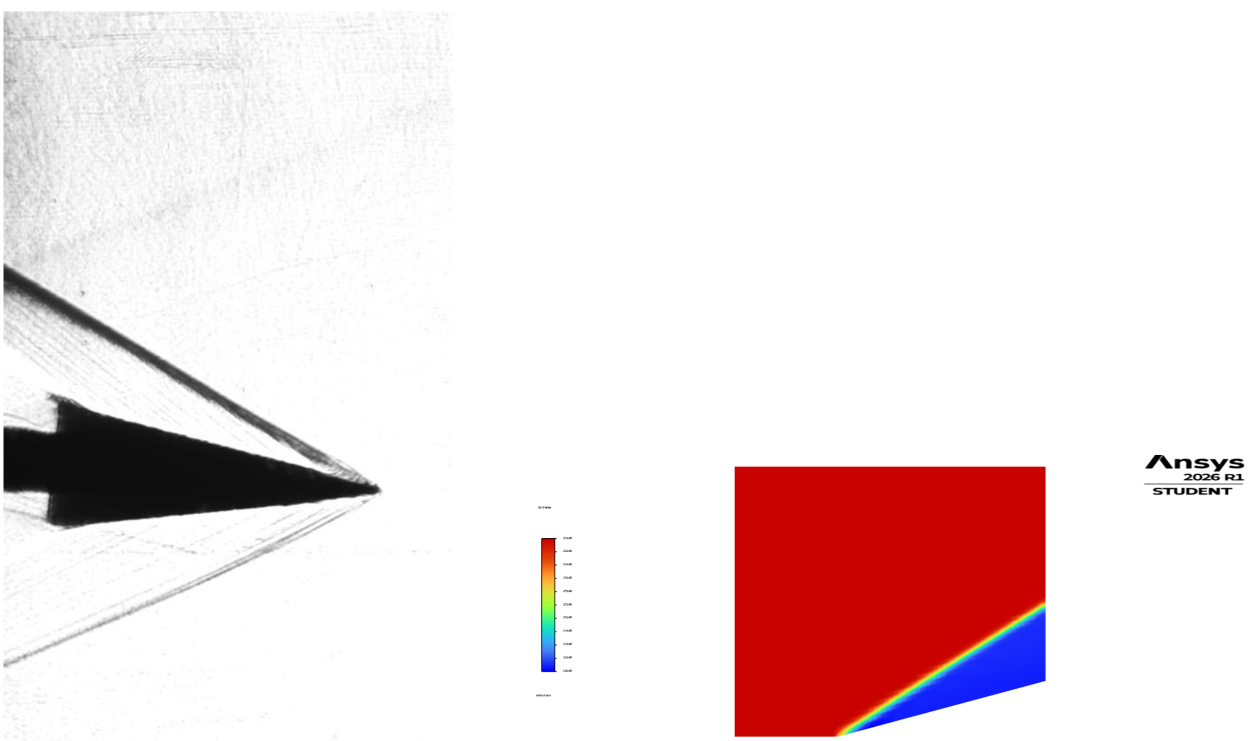

Schlieren image CFD Mach contour

Fig. 10 Schlieren and CFD comparison for $M_1 = 3.0$ and $\theta = 15°$.

G. Discussion of Trends

For a fixed freestream Mach number, the shock angle increases as the wedge half-angle increases. This occurs because a larger wedge angle requires a stronger flow deflection, causing the attached shock to stand at a larger angle relative to the freestream. For a fixed wedge half-angle, the shock angle decreases as Mach number increases because the Mach angle decreases and the shock leans closer to the wedge surface.

The CFD measurements agree closely with theory because the shock is well-defined in the Mach number contours. The experimental angles show the same general trend but have larger deviations. These deviations are expected because the Schlieren shock band has finite thickness, the shock near the wedge tip can be blurred, and the apparent centerline of the shock can shift depending on contrast and image exposure.

V. Conclusion

This report compared oblique shock angles for supersonic flow over a two-dimensional wedge at $M_1 = 2.0$, 2.5, and 3.0 with wedge half-angles of 5°, 10°, and 15°. The analytical values were calculated using the weak-shock branch of the θ–β–M relation. CFD shock angles were measured from the Mach contour transition bands and were found to match the analytical predictions closely. The Schlieren measurements followed the correct trend but showed larger scatter because of image-based measurement uncertainty. Overall, the comparison confirms the expected oblique-shock behavior: increasing wedge half-angle increases β, while increasing freestream Mach number decreases β for the same wedge half-angle.

Appendix A: Representative Hand Calculation

For the case $M_1 = 2.5$, $\theta = 10°$, $p_1 = 101\,325\,\mathrm{Pa}$, and $T_1 = 300\,\mathrm{K}$, the weak-shock solution is

$$\beta = 31.85°.$$

The upstream normal Mach number is

$$M_{n1} = M_1 \sin\beta = 2.5 \sin(31.85°) = 1.319.$$

The pressure ratio is

$$\frac{p_2}{p_1} = 1 + \frac{2(1.4)}{1.4+1}\left(1.319^2 - 1\right) = 1.864,$$

so that

$$p_2 = (1.864)(101\,325\,\mathrm{Pa}) = 188\,857\,\mathrm{Pa}.$$

The same sequence is repeated for density ratio, temperature ratio, downstream normal Mach number, and downstream Mach number using Eqs. (4)–(7).

Appendix B: Computational Grids

The initial solution produced a Mach contour in which the oblique shock appeared smeared, making the transition in Mach number difficult to distinguish. To improve the numerical resolution of the shock, the mesh was manually refined in the region of high pressure gradient surrounding the oblique shock. Increasing the cell density across the minimum-to-maximum pressure-gradient region allowed the solver to better capture the sharp flow-property change across the shock, producing a clearer Mach number transition in the final contour.

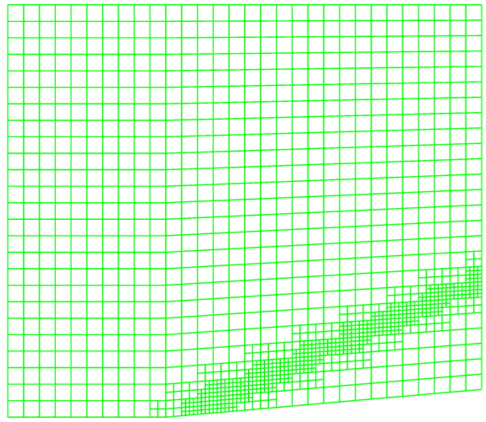

Fig. 11 Computational grid used for $M_1 = 3.0$ and $\theta = 5°$.

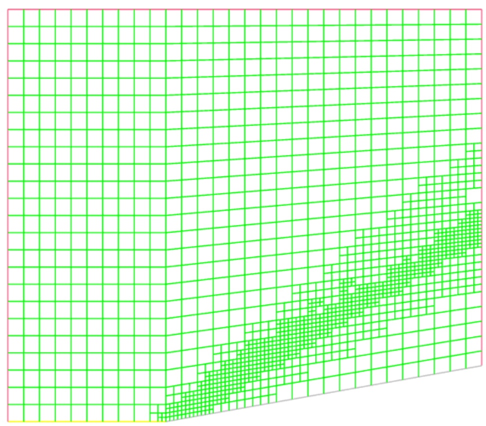

Fig. 12 Computational grid used for $M_1 = 2.0$ and $\theta = 10°$.

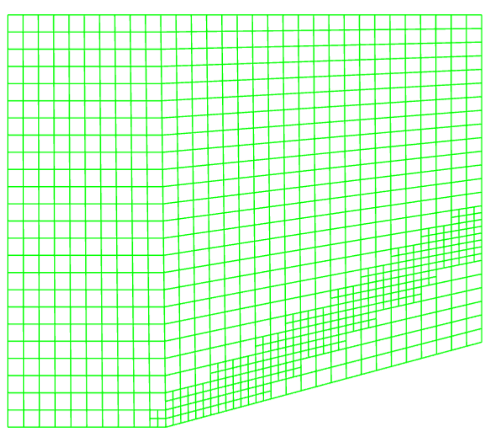

Fig. 13 Computational grid used for $M_1 = 3.0$ and $\theta = 15°$.

Appendix C: Reference θ–β–M Chart

CHAPTER 9 Oblique Shock and Expansion Waves

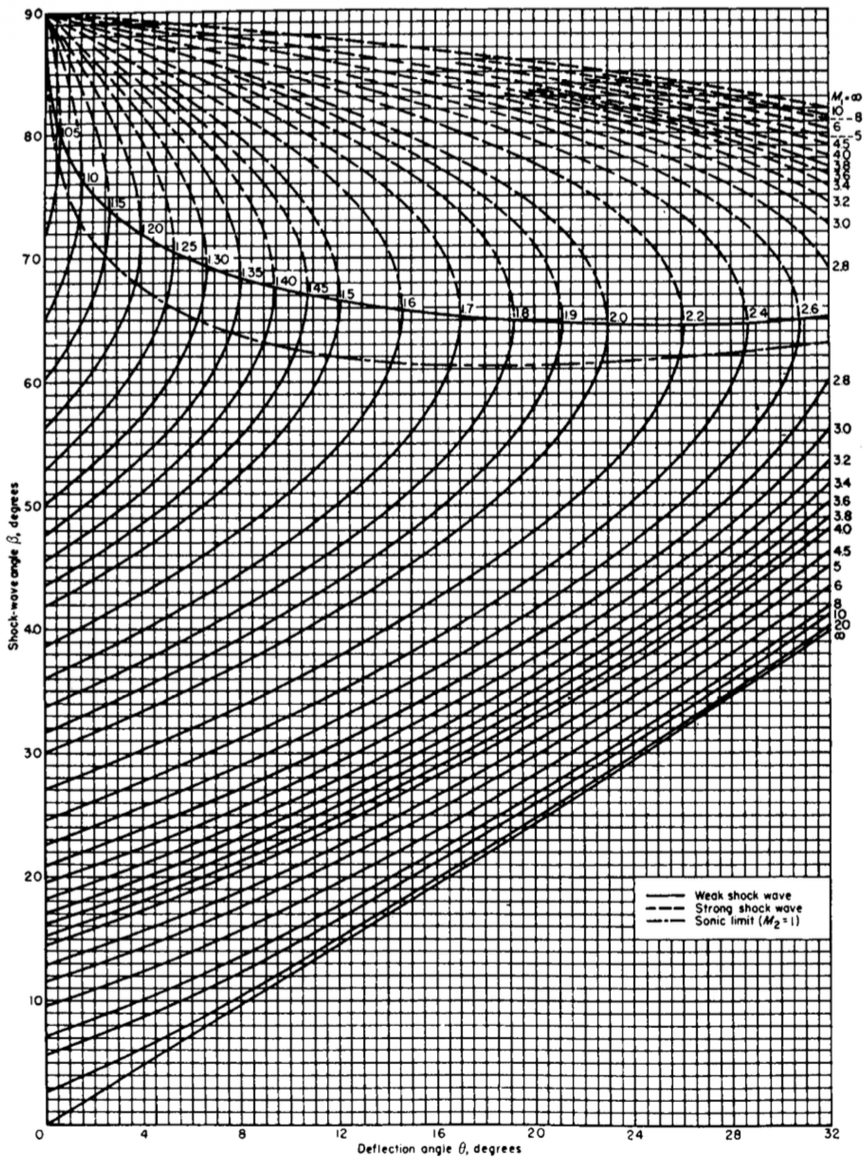

(*a*)

Figure 9.9 Oblique shock properties: $\gamma = 1.4$. The θ-β-M diagram. (*Source: NACA Report 1135, Ames Research Staff, "Equations, Tables and Charts for Compressible Flow," 1953.*)

Fig. 14 Reference θ–β–M chart used as a graphical check for the theoretical shock angles.

References

[1] EAE 198 Compressible Flow Aerodynamics, "Project – Shock Wave Analysis," University of California, Davis, 2026.

[2] Anderson, J. D., *Modern Compressible Flow: With Historical Perspective*, McGraw-Hill, New York.